High-Visibility, High-Strength, Rapid-Response, In-Fiber Optofluidic Sensor

Qiang Zhang, Zongyang Li, Xinzhang Tian, Pengli Hao, Xuyang Wang, and Yongmin Li

***Abstract*—Optofluidic sensors are promising tools in biological and chemical analysis. A challenge for optofluidic sensors in most practical applications is to have simultaneously high visibility, high mechanical strength, and rapid response for high-resolution, stable, and fast measurement. Here, we demonstrated an optofluidic sensor by splicing a hollow-core fiber (HCF) between a suspended-core fiber (SCF) and a single-mode fiber. By establishing the heat-conduction theoretical model of the SCF, an undeformed high-strength splicing technique was proposed. The undeformed splicing can eliminate the curvature of the end face of the core in the SCF, which is crucial to attain a high-visibility Fabry-Pérot cavity. Experimental results showed that the fringe visibility was up to 28 dB in air and 22 dB in water. Meanwhile, the measured mechanical strength of the splicing joint by the splicing technique reached to 30.02 kpsi, which is close to that of the HCF (37.84 kpsi) or SCF (39.45 kpsi). Moreover, the response time of this sensor was less than 1.5 s, and the refractive index sensitivity was 1153.74 nm/RIU. Therefore, the proposed sensor is a promising candidate in practical biological and chemical measurements.**

***Index Terms*—Fabry–Pérot interferometers, optical fiber sensors, optofluidics.**

I. Introduction

OPTOFLUIDICS integrates the fields of optics and fluidics, and provides promising biological and chemical analytic capabilities [1]–[5]. Optofluidic sensors based on an in-fiber open-cavity Fabry–Pérot (IFOCFP) cavity have several advantages such as easy light coupling, compactness, low transmission loss, low temperature dependence, and direct interaction access for analyte samples and light. One of the conventional methods for fabricating IFOCFP cavities is to use a femtosecond laser [6]–[9] or focused-ion beam [10]–[15]. The surface machined by this technique needs to be smoothed further for high visibility, and the machining equipment is expensive [6], [19], [20]. In our previous work, an IFOCFP cavity based the side-polished technique was proposed that decreases the manufacturing cost and optimizes the fringe visibility, although the fabrication process is complex [16]. A simple alternative method is to directly form IFOCFP cavities using special optical fibers, such as lateral offset-splicing fiber [17], microstructured fibers [18], [19], C-shaped fiber [20], and microfibers [21], [22]. However, the C-shaped fiber is a noncommercial component and the sensors based on offset-splicing fiber or microfibers suffer weak mechanical strength [20], [22]. On the other hand, the sensors based on microstructured fibers require auxiliary pump equipment to direct the fluid into and out of the sensors because of the small air holes in the cladding [20]. In the practical applications, an optofluidic sensor that simultaneously offers high fringe visibility, high mechanical strength, and a short response time is attractive and desirable for high-resolution, stable, and fast measurement.

In this work, we propose a high-visibility high-strength rapid-response IFOCFP optofluidic sensor by splicing a hollow-core fiber (HCF) between a suspended-core fiber (SCF) and a single-mode fiber (SMF). The end faces of the SCF and SMF form an optical Fabry–Pérot (FP) cavity. To improve the fringe visibility and mechanical strength of the sensor, an undeformed high-strength splicing technique for the HCF and SCF was proposed and demonstrated experimentally by analyzing the temperature field model of the arc discharge between two electrodes and optimizing the parameters of arc discharge. The undeformed splicing technique for the HCF and SCF can effectively eliminate the curvature of the end face of the core in the SCF. In this case, a high fringe visibility in the two-beam FP interferometer is obtained due to nearly balanced lights reflected into the lead-in fiber. Experimental results showed that the fringe visibility of the sensor is up to 28 dB in air and 22 dB in water, which is consistent with the highest value in reported proposals without high reflective film [21]. Another advantage of the sensor is the high mechanical strength, which reaches 30.02 kpsi and is close to that of the HCF (37.84 kpsi) or SCF (39.45 kpsi). Furthermore, the response time of this sensor with a 35-μm length SCF is less than 1.5 s, owning to the six 32-μm-diameter holes in the cladding of the SCF and the undeformed splicing technique. Moreover, the sensor is compact, easy to fabricate, and insensitive to ambient temperature (1.37 pm/°C in air). Therefore, the proposed sensor is a promising candidate for biological and chemical application.

Manuscript received December 19, 2017; revised March 9, 2018 and March 30, 2018; accepted April 15, 2018. Date of publication April 20, 2018; date of current version May 31, 2018. This work was supported in part by the Key Project of the National Key R&D Program of China under Grant 2016YFA0301403, in part by the Natural National Science Foundation of China under Grants 11774209 and 61378010, in part by the Shanxi 1331KSC, and in part by the Program for the Outstanding Innovative Teams of Higher Learning Institutions of Shanxi. *(Corresponding author: Yongmin Li.)*

The authors are with the State Key Laboratory of Quantum Optics and Quantum Optics Devices, the Institute of Opto-Electronics and the Collaborative Innovation Center of Extreme Optics, Shanxi University, Taiyuan 030006, China (e-mail: qzhang@sxu.edu.cn; leonard1989@foxmail.com; 330834081@qq.com; 345365629@qq.com; wangxuyang@sxu.edu.cn; yongmin@sxu.edu.cn).

Color versions of one or more of the figures in this paper are available online at http://ieeexplore.ieee.org

Digital Object Identifier 10.1109/JLT.2018.2828847

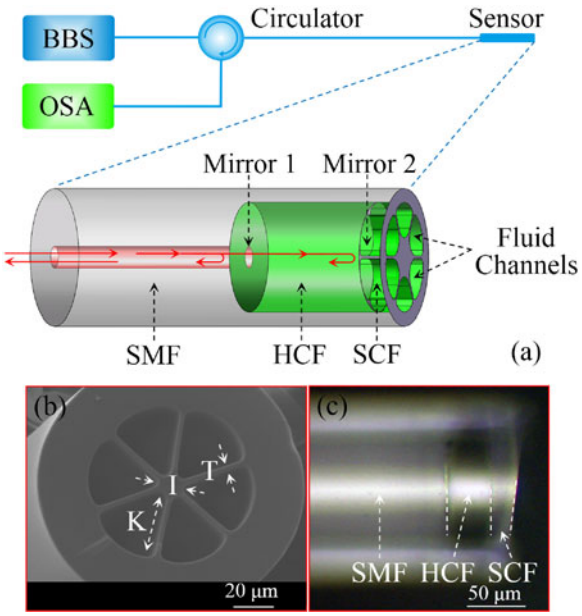

Fig. 1. (a) Schematic of the IFOCFP optofluidic sensor system (BBS: broadband source; OSA: optical spectrum analyzer); (b) SEM image of the SCF; (c) side view of the sensor, the lengths of the HCF and SCF are 46 and 35 μm, respectively.

II. Fabrication and Principle

A. Structure of the Sensor

A schematic of the proposed IFOCFP optofluidic sensor is shown in Fig. 1(a). An HCF is spliced between an SMF and an SCF. The lengths of the HCF and SCF can be tailored precisely under a microscope. The end faces of the SMF and SCF form a FP interferometer. A scanning electron microscope (SEM) image of the SCF is shown in Fig. 1(b). The SCF was purchased from FiberHome Technologies and has a 13-μm-diameter core surrounded by six holes with a diameter *K* of 32 μm. The thickness *T* of the silica beams between the air holes is 2.2 μm, and the outer diameter of the fiber is 125 μm. The HCF has an inner diameter of 77 μm and outer diameter of 125 μm.

B. Principle

As shown in Fig. 1, the incident light is reflected by the end faces of the SMF and SCF to generate a two-beam FP interference pattern, where the other end face of the SCF is polished with an 8° inclination to eliminate the reflected light, as shown in Fig. 1(c). The normalized reflection spectrum I_{FP} of the IFOCFP cavity is:

$$\begin{aligned} I_{FP} &= R_1 + (1-\alpha_1)^2 (1-\alpha_2) (1-\gamma)^2 (1-R_1)^2 R_2 \\ &\quad + 2\sqrt{\mathrm{R_1 R_2}\,(1-\alpha_2)}\,(1-\alpha_1)\,(1-\gamma)\,(1-\mathrm{R_1}) \\ &\quad \times \cos\left(4\pi n_{an} L/\lambda + \pi\right), \end{aligned} \tag{1}$$

where λ is the wavelength of the incident beam; α_{i} is the attenuation factors at mirrors i ($i = 1, 2$) resulting from the rough surfaces; γ and L are the transmission loss and cavity length of the cavity, respectively; and R_{i} is the reflection coefficients at mirrors i:

$$R_1 = R_2 = (n_{co} - n_{an})^2 / (n_{co} + n_{an})^2, \tag{2}$$

where n_{co} and n_{an} are the refractive index (RI) of the core in the optical fiber and the sample, respectively, and π is the half-wave loss from Mirror 1 ($n_{\mathrm{an}} > n_{\mathrm{co}}$) or Mirror 2 ($n_{\mathrm{an}} < n_{\mathrm{co}}$).

From (1), the *m*th order interference dip λ_{m} of the destructive interference in the FP cavity can be calculated by the formula:

$$m\lambda_m = 2Ln_{an}. \tag{3}$$

According to (1), the fringe visibility *V* is given by

$$\begin{aligned} V &= \frac{I_{FP\max} - I_{FP\min}}{I_{FP\max} + I_{FP\min}} \\ &= \frac{2\,(1-\alpha_1)\,\sqrt{1-\alpha_2}\,(1-\gamma)\,(1-R_1)}{1 + \left[(1-\alpha_1)\,\sqrt{1-\alpha_2}\,(1-\gamma)\,(1-R_1)\right]^2}. \end{aligned} \tag{4}$$

From (4), one can improve the fringe visibility *V* of the FP cavity by decreasing α_1, α_2, and γ simultaneously.

C. Undeformed High-Strength Splicing Technique

In this two-beam interference sensor, the fringe visibility is decided by the relative intensities of the two reflected lights from Mirrors 1 and 2, and is maximum when the light intensities of the reflected lights are equal. Therefore, α_{i} and γ need to be decreased simultaneously to improve the fringe visibility of the sensor. The surface tension will smooth the end faces of the fibers during the arc-discharge splicing progress and eliminate the attenuation factors α_{i}. The γ value is proportional to the cavity length and the diffuse angle at the reflective mirrors. A conventional splicing technique will result in the fibers having a convex end face and aggravate γ [23]. Therefore, an undeformed robust splicing technique for the SMF, HCF, and SCF is essential for a high-visibility high-strength sensor. The undeformed high-strength splicing joint for the SMF and HCF can be obtained using the large offset reheating method [24]. However, this method is unsuitable for splicing the HCF and SCF, because a serious collapse will occur in the one that has a higher temperature than the other. Therefore, an undeformed high-strength splicing technique for the HCF and SCF must be researched further.

1) Splicing Method: To obtain undeformed high-strength splicing of the HCF and SCF, we simulated the distributions of the current density and temperature of the arc discharge between the two electrodes using the finite element method (FEM). In the simulation, bilateral same conical electrodes were designed with a tip diameter of 0.1 mm, base diameter of 2.0 mm, length of 3.5 mm, and air gap of 2.0 mm. The parameters of the electrodes are from the FITEL S183ver.2 fusion splicer used in our experiment, and the arc current was 19 mA. The contour lines in Fig. 2 depict distributions of the current density and temperature between the two electrodes. As shown in Fig. 2(a) and (b), the temperature distribution between the electrodes is similar to that of the current density. The temperature is highest at the tips of the electrodes and falls to a minimal value in the middle between the two conical electrodes in the X-Z plane, and is Gaussian in the X-Y plane in Fig. 2(c). Fig. 1(d) presents the normalized

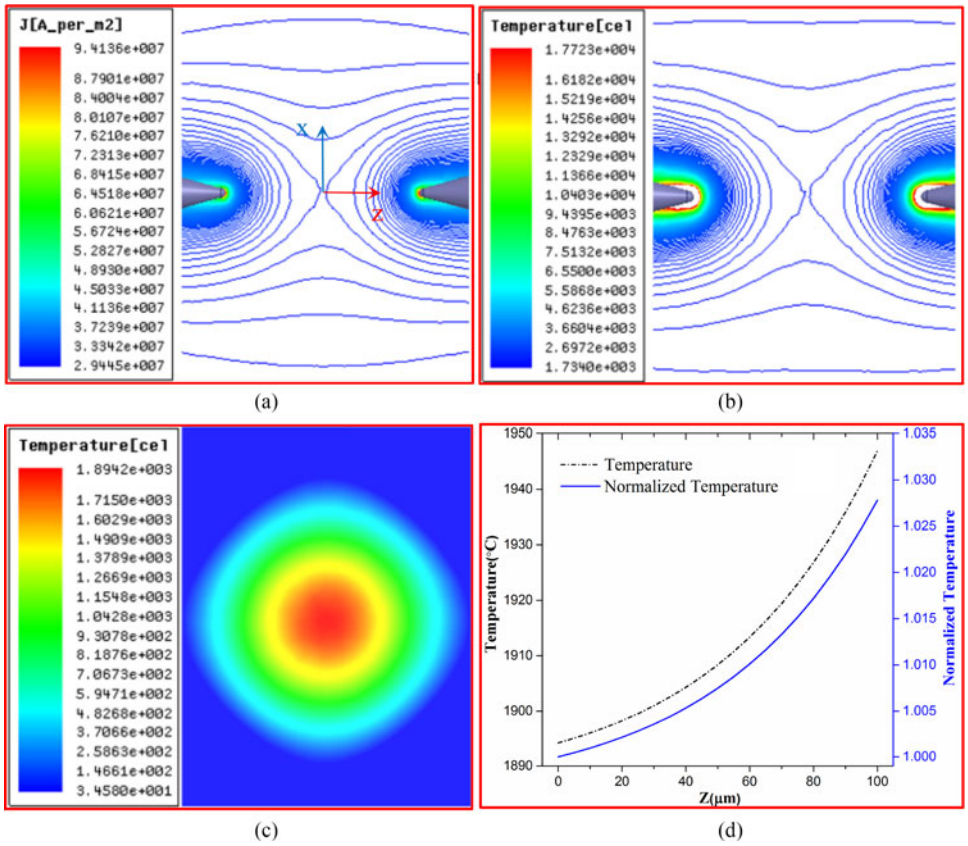

Fig. 2. Distributions of current density (a) and temperature (b) between the electrodes by contour lines in X-Z plane; (c) temperature distribution between the electrodes in X-Y plane and (d) temperature evolution with the *Z* increasing from 0 to 100 μm.

temperature increases from 1 to 1.028 as the *Z* increases from 0 (the midpoint between the electrodes) to 100 μm. The simulated results are consistent with the experimental data [25], [26].

Hence, when an optical fiber is placed in the middle of the electrodes, the temperature of the core is lower than that of the outer cladding without considering the heat conduction in the fiber. For an SMF, the time required to establish a uniform temperature field between the outer cladding and core, which is defined as the heat conduction time t_{SMF}, can be expressed as follows [27]:

$$t_{SMF} = D_{fiber}^2/4\alpha, \tag{5}$$

where D_{fiber} is the diameter of the fiber, α is the heat-diffusivity coefficient of the fiber which is 1.4×10^{-6} m^2/ s. Thus, only 2.8 millisecond (msec) is required to establish a uniform temperature field in an SMF.

However, for the SCF in our experiments, the heat conduction from the outer cladding to the core is much slower than t_{SMF} due to the air holes. The heat conduction model includes three parts: the outer cladding, the air hole cladding and the core. Therefore, the heat conduction time is given by

$$t_{SCF} = t_{outer} + t_{hole} + t_{core}. \tag{6}$$

According to the (5), the heat conduction time t_{outer} of the outer cladding in the SCF may be expressed as follows:

$$t_{outer} = \left(D_{fiber}^2 - D_{hole}^2\right)/4\alpha, \tag{7}$$

where $D_{\text{hole}} = I + 2K$ is the outer diameter of the air hole cladding, and thus the corresponding t_{outer} is 1.7 msec. The heat conduction time t_{core} of the core in the SCF may be calculated as:

$$t_{core} = I^2/4\alpha, \tag{8}$$

in our experiments, the diameter of the core *I* is 13 μm, and thus the t_{core} is 0.03 msec. The heat conduction time t_{hole} of the air hole cladding needs to be analyzed further. The rate of heat flow through the micro beams between the air holes can be described by Fourier's Law:

$$Q(t) = -kA\left(T_{core}(t) - T_{outer}\right)/K, \tag{9}$$

where T_{core} and T_{outer} are the temperatures of the fiber core and the outer cladding in the SCF, respectively, *k* is thermal conductivity, $A = 6Td$ is area of heat flow, and *d* is the characteristic width of the heated zone. The relationship of the heat *W* flowing into the beams and T_{core} can be expressed as:

$$W = cm\left(T_{core} - T_0\right), \tag{10}$$

where c is the fiber heat capacity, m and T_0 are the mass and initial temperature of the beams and the core, respectively. During the time d*t*, the heat flowing into the beams is $W_{\text{dt}} = \text{Q(t)d}t$, and the temperature change of the beams and

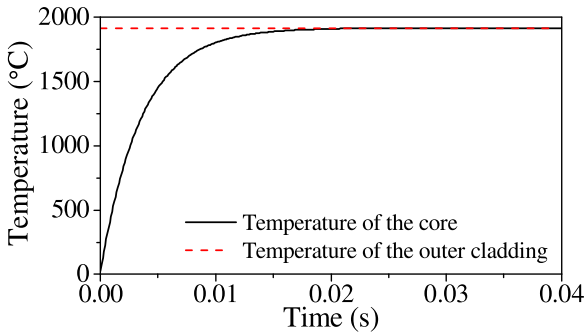

Fig. 3. Temperature of the core in the SCF with increasing the arc duration.

core is $dT_{core} = W_{dt}/\text{cm}$. Thus, the heat flow rate change

$$\begin{aligned} dQ(t) &= Q(t+dt) - Q(t) \\ &= -kAdT_{core}/K \\ &= -kAQ(t)\,\mathrm{d}t/Kcm. \end{aligned} \tag{11}$$

Integrating the (11), the rate of heat flow can be given as

$$Q(t) = Exp(C_1 - kAt/Kcm), \tag{12}$$

where C_1 can be calculated by substituting Q(0):

$$C_1 = \ln\left[-kA(T_0 - T_{outer})/K\right]. \tag{13}$$

Then, the T_{core}(t) can be expressed as

$$T_{core}(t) = T_{outer} - (T_{outer} - T_0)\,Exp(-kAt/Kcm). \tag{14}$$

Fig. 3 shows the temperature T_{core} as the arc duration increases with $k = 0.7\,\text{W/m}-\text{K}$, $m = \rho(d\pi I^2/4 + AK)$, $\rho = 2.2 \times 10^3\,\text{kg/m}^3$, $K = 32\,\mu\text{m}$, $c = 840\,\text{J/kg}-\text{K}$, T_{outer} is 1915 °C according to Fig. 2, and T_0 is room temperature 25 °C due to a higher breakdown voltage of SiO_2. The T_{core} will surpass 1910 °C when the arc duration is 21 msec.

The temperature of the core in the SCF is always lower than that of the outer cladding when the arc duration is less than t_{SCF}. This phenomenon can be used to fabricate an undeformed high-strength splicing joint between the HCF and SCF. First, an undeformed low-strength splicing joint for the HCF and SCF can be fabricated by decreasing the power and duration of the arc discharge. Then, additional arc discharges with a duration on the order of the t_{SCF} (Considering the time to melt the outer cladding) can be utilized to strengthen the undeformed low-strength splicing joint.

2) Step One: Fabricating an Undeformed Low-Strength Splicing Joint: In our experiment, a FITEL S183ver.2 fusion splicer was used to splice the fibers. The typical parameters for splicing SMFs in customized programs of the fusion splicer are the arc power 100, and fusion time 1.0 s. Optimal parameters for undeformed low-strength splicing of the HCF and SCF may be achieved by scaling the duration and power of arc discharge to monitor the air-hole deformation of the SCF.

Fig. 4 shows side views and end faces of the SCFs when the arc power was 70 and the arc duration varied from 0.11 s to 0.14 s in steps of 0.01 s. The side views had no obvious deformation from increasing the arc duration. However, obvious changes in

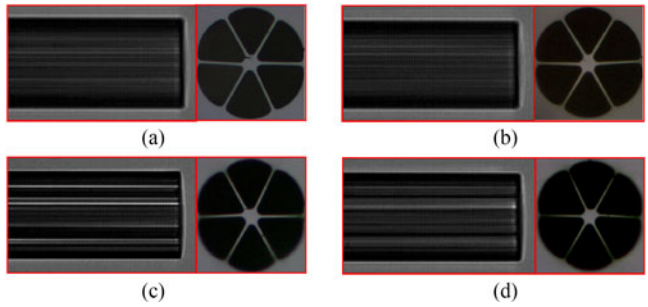

Fig. 4. Side views and end faces of the SCFs with different durations: (a) 0.11 s, (b) 0.12 s, (c) 0.13 s, (d) 0.14 s, and the power was 70.

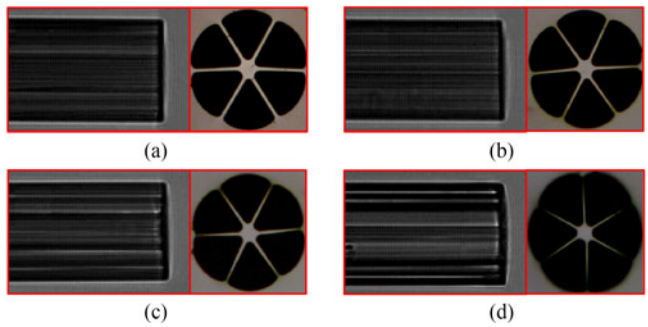

Fig. 5. Side views and end faces of the SCFs with different power: (a) 60, (b) 70, (c) 80, (d) 90 and the duration was 0.12 s.

the end faces of the SCF appeared. First, the beam thickness T decreased from 2.2 μm to ~1.5 μm as the arc duration increased from 0.11 s to 0.14 s. The reason why T decreases is that the surface tension under higher temperature causes the periphery of the beams to cave in. Second, the contact parts between the beams and outer cladding were more obscured than that between the beams and inner cladding. This can be explained as follows: the temperature of the SiO_2 cladding is higher than that of the core in the SCF, so the deformation resulting from the surface tension is more obvious in the contact parts between the beams and outer cladding. The results agree with the analysis in the previous section. Meanwhile, it can be seen that it is more accurate to value the deformation by monitoring the end face evolution of the SCF than by monitoring the side views evolution with different arc discharges.

We also investigated the effect of changing the arc power when the arc duration was constant. Fig. 5 shows the side views and end faces of the SCFs when the arc duration was 0.12 s and the arc power varied from 60 to 90. Experimental results were similar to that by varying the arc duration with constant arc power. When the arc power increased from 60 to 90, the T of the beams decreased from 2.2 μm to ~1.4 μm, and the deformation of the contact parts between the beams and SiO_2 cladding was more serious than that of the contact parts between the beams and core. Therefore, in our experiment the power and duration of the arc used to fabricate an undeformed low-strength splicing joint were 70 and 0.12 s, respectively. Moreover, the deformation of HCF was similar to that of the SCF due to the same size and material between them.

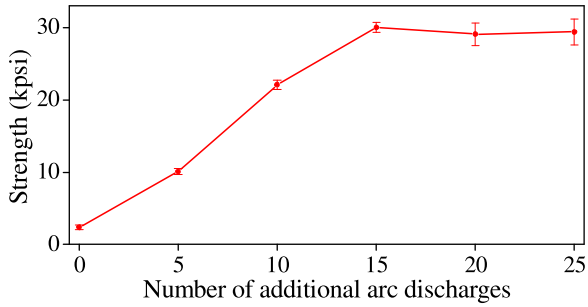

Fig. 6. The relationship between the mechanical strength and the number of additional arc discharges.

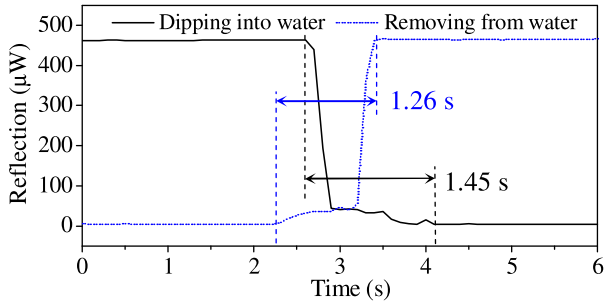

Fig. 8. Response times of the sensor dipped into and removed from deionized water.

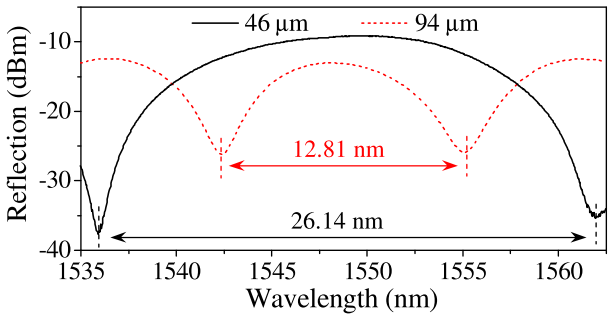

Fig. 7. Reflection spectra of the IFOCFP optofluidic sensors with cavity lengths of 46 and 94 μm in air.

3) Step Two: Strengthening the Undeformed Low-Strength Splicing Joint: The splicing joint fabricated by the optimized splicing procedure described above was undeformed but fragile, and should be strengthened further by additional arc discharges. According to Fig. 4, there is no obvious deformation in the end faces of the SCF when the arc duration is 0.11 s. Therefore, the additional arc with 0.03 s duration and 70 power was used to strengthen the fragile splicing point in our experiments. We measured the mechanical strength of the splicing joint formed by this splicing technique as the number of additional arc discharges increased. As shown in Fig. 6, when the number of additional arc discharges was increased to 15, the tensile strength reached the peak at 30.02 kpsi, and was saturated as the number increased further. Experimental results showed the mechanical strength of the splicing joint is close to that of the SCT (37.84 kpsi) or SCOF (39.45 kpsi).

III. Results and Discussions

A. Reflection Spectra of the Sensors in Air

We measured the reflection spectra of the IFOCFP optofluidic sensors. A schematic of our design is shown in Fig. 1(a). Light from a BBS with a wavelength range of 1520–1620 nm was launched into the proposed sensor through a circulator, and an OSA (type: OSA203, Thorlabs) was utilized to analyze the reflection spectrum of the sensor. Fig. 7 shows the observed interference fringes in the reflection spectra of the IFOCFP optofluidic sensors. The free spectrum ranges (FSRs) of the interference fringes were 26.14 and 12.81 nm, thus, the cavity lengths $L = \lambda_m^2/2n_{an}$FSR were approximately 46 and 94 μm, respectively. We can see that the fringe visibility of the sensor with $L = 46\,\mu$m was up to 28 dB in air, which is consistent with the highest value in reported proposals without high reflective film [21]. When the cavity length increases to 94 μm, the fringe visibility of the sensor falls to 13 dB because of the increase of the diffraction loss and modes mismatch loss. It is noted that the angle of the cleave facet should be less than 0.4° for a stable high than 20 dB fringe visibility.

B. Response to RI

We investigated the response of the IFOCFP optofluidic sensor to the RI by using refractive index matching liquids. The IFOCFP optofluidic sensor was immersed in the fluids at a small inclination (≈5°) between the horizontal line and axis of the device. In our experiments, the proposed sensor was carefully cleaned with deionized water and alcohol in an ultrasonic bath to eliminate residual fluids within the FP cavity, such that the original spectrum in air was recovered after each test. This was used to gain standard reflection spectra and is unnecessary in practical applications. Experimental results showed that the fluids can rapidly access the optofluidic cavity and interact with the light without an auxiliary pump equipment to direct the fluids because of the six large holes with diameters of 32 μm in the SCF and the undeformed splicing technique for the HCF and SCF. As shown in Fig. 8, the response times of the sensor dipped into and removed from deionized water was 1.45 and 1.26 s, respectively.

The response of the IFOCFP optofluidic sensor to different RIs is shown in Fig. 9(a). The fringe visibility of the device with $L = 46\,\mu$m was up to 22 dB, which is higher than that in reported proposals without high reflective film. Fig. 9(a) shows that the λ_m gradually increased (redshift) when the RI of the fluid increased from 1.333 to 1.345.

To analyze the sensitivity of the IFOCFP optofluidic sensor, we traced the change of λ_m (1529.57 nm) with different RIs of the fluid in the cavity. Fig. 9(b) plots the λ_m as a function of the RI value for the filled fluid. Linear fitting was employed to determine the RI sensitivity of the sensor, and experimental results showed that the RI sensitivity was 1153.74 nm/RIU which is comparable to that of other IFOCFP refractometers [8], [10], [19], [21]. According to (3), the simulated sensitivity at an RI of 1.333 is 1147.50 nm/RIU, which is close to the measured

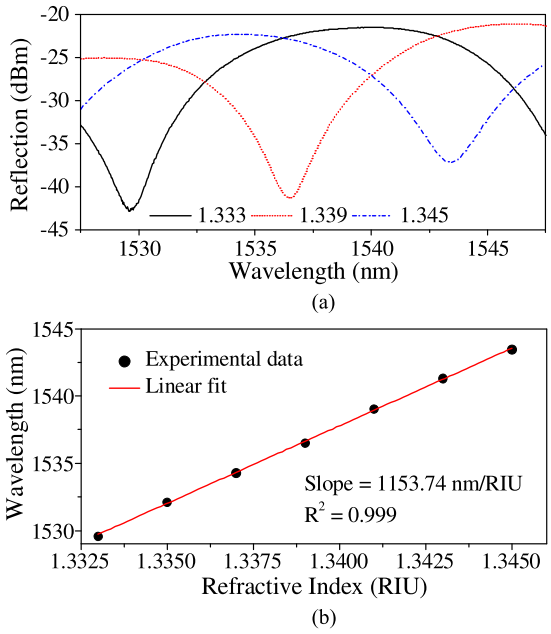

Fig. 9. (a) Reflection spectra, and (b) λ_m evolution of the sensor with RIs from 1.333 to 1.345.

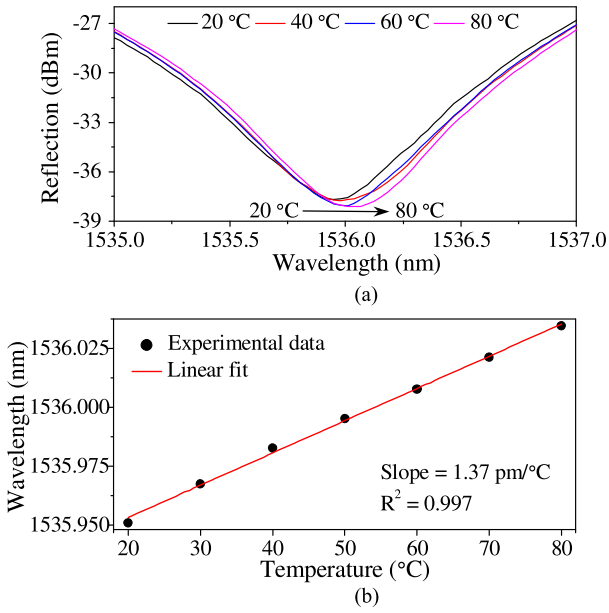

Fig. 10. (a) Reflection spectrum and (b) λ_m evolution of the IFOCFP sensor in air with the temperature changing from 20 °C to 80 °C.

sensitivity. Similar experimental phenomena were obtained for other sensors with different parameters.

C. Response to Temperature Variation in Air

We further investigated the response of the proposed sensor to the ambient temperature change in air. As shown in Fig. 1(a), the L value of the sensor is given by the distance between the end faces of the SMF and SCF. When subjected to a temperature change ΔT, there is a change in L, expressed as $\Delta L = L\beta\Delta T$. Here, β is the thermal expansion coefficient of the HCF. According to (3), the dip wavelength shift $\Delta\lambda$ with ΔT is given by

$$\Delta\lambda = \lambda_m \beta \Delta T. \tag{15}$$

Fig. 10 shows that the reflection spectra of the IFOCFP sensor shifted slightly to a longer wavelength as the ambient temperature increased from 20 °C to 80 °C. The dip wavelength (1535.95 nm) of the sensor increased linearly with the temperature at a sensitivity of 1.37 pm/°C, which is close to the theoretical sensitivity of 0.86 pm/°C obtained from (7) ($\beta \approx 0.56 \times 10^{-6}/°C$). Thus, this device is insensitive to the surrounding temperature in air.

D. Response to Temperature Variation in Deionized Water

To investigate how the temperature variance affects the sensing performance in a liquid environment, the proposed optofluidic sensor with $L = 46\,\mu$m was immersed in deionized water. The reflection spectra in Fig. 11(a) show a blue shift when increasing the temperature of the deionized water. As shown in Fig. 11(b), the dip wavelength of the proposed IFOCFP optofluidic sensor decreased linearly with a slope of -0.1134 nm/°C, which agrees with the calculated value -0.1147 nm/°C (the water refractive index change corresponds to approximately $10^{-4}{}^{\circ}\mathrm{C}^{-1}$) according to (3).

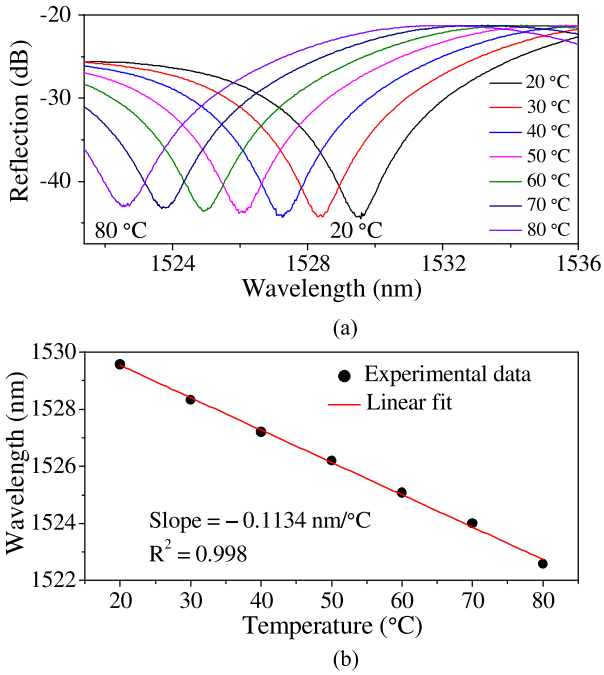

Fig. 11. (a) Reflection spectrum and (b) λ_m evolution of the IFOCFP optofluidic sensor in deionized water with the temperature changing from 20 °C to 80 °C.

In-fiber FP optofluidic sensors based on PCF have several advantages such as simple fabrication process and low cost, and are more suitable for practical applications. Compared with other FP sensors based on PCF [18], the proposed sensor has similar RI sensitivity, but shorter response time. Furthermore, it does not need auxiliary pump equipment to direct the fluid into

and out of the sensors due to the six 32-μm-diameter holes in the SCF and the undeformed splicing technique.

IV. Conclusion

In this work, we designed a high-visibility high-strength rapid-response IFOCFP optofluidic sensor by splicing an HCF and SCF to an SMF with an optimized splicing technique. The optical FP cavity formed by the end faces of the SMF and SCF functions as a fluidic cavity. Experimental results showed that the proposed sensor exhibits high fringe visibility and mechanical strength. To demonstrate the functionality of this device, the sensor was used to measure different RIs. The experimental results showed that the response time was short and that the RI response was approximately linear with the sensitivity of 1153.74 nm/RIU in the range of 1.333–1.345. These features indicate that the proposed sensor is a promising candidate in biological and chemical applications.

References

[1] D. Psaltis, S. R. Quake, and C. Yang, "Developing optofluidic technology through the fusion of microfluidics and optics," *Nature*, vol. 442, pp. 381–386, Jul. 2006.

[2] X. Fan and I. M. White "Optofluidic microsystems for chemical and biological analysis," *Nature Photon.*, vol. 5, pp. 591–597, Sep. 2011.

[3] L. Pang, H. M. Chen, L. M. Freeman, and Y. Fainman, "Optofluidic devices and applications in photonics, sensing and imaging," *Lab Chip*, vol. 12, pp. 3543–3551, May 2012.

[4] C. Zhang *et al.*, "Microbubble-based fiber optofluidic interferometer for sensing," *J. Lightw. Technol.*, vol. 35, no. 13, pp. 2514–2519, Apr. 2017.

[5] C. Gong *et al.*, "Fiber optofluidic microlaser with lateral single mode emission," *IEEE J. Sel. Topics Quantum Electron.*, vol. 24, no. 4, Jul./Aug. 2018, Art. no. 0900206.

[6] Y. Rao, M. Deng, D. Duan, X. Yang, T. Zhu, and G. Cheng, "Micro Fabry–Perot interferometers in silica fibers machined by femtosecond laser," *Opt. Express*, vol. 15, no. 21, pp. 14123–14128, Oct. 2007.

[7] C. R. Liao, T. Y. Hu, and D. N. Wang, "Optical fiber Fabry–Perot interferometer cavity fabricated by femtosecond laser micromachining and fusion splicing for refractive index sensing," *Opt. Express*, vol. 20, no. 20, pp. 22813–22818, Sep. 2012.

[8] M. Tian, P. Lu, L. Chen, D. Liu, M. Yang, and J. Zhang, "Femtosecond laser fabricated in-line micro multicavity fiber FP interferometers sensor," *Opt. Commun.*, vol. 316, pp. 80–85, Dec. 2014.

[9] L. Yuan, J. Huang, X. Lan, H. Wang, L. Jiang, and H. Xiao, "All-in-fiber optofluidic sensor fabricated by femtosecond laser assisted chemical etching," *Opt. Lett.*, vol. 39, no. 8, pp. 2358–2361, Apr. 2014.

[10] C. J. Alberts, S. de Man, J. W. Berenschot, V. J. Gadgil, M. C. Elwenspoek, and D. Iannuzzi, "Fiber-top refractometer," *Meas. Sci. Technol.*, vol. 20, Feb. 2009, Art. no. 034005.

[11] W. Yuan, F. Wang, A. Savenko, D. H. Petersen, and O. Bang, "Note: Optical fiber milled by focused ion beam and its application for Fabry–Pérot refractive index sensor," *Rev. Sci. Instrum.*, vol. 82, Jul. 2011, Art. no. 076103.

[12] T. Wieduwilt, J. Dellith, F. Talkenberg, H. Bartelt, and M. A. Schmidt, "Reflectivity enhanced refractive index sensor based on a fiber-integrated Fabry–Perot microresonator," *Opt. Express*, vol. 22, no.21, pp. 25333–25346, Oct. 2014.

[13] J. Li *et al.*, "Fabricating optical fibre-top cantilevers for temperature sensing," *Meas. Sci. Technol.*, vol. 25, Feb. 2014, Art. no. 035206.

[14] S. C. Warren-Smith, R. M. André, J. Dellith, T. Eschrich, M. Becker, and H. Bartelt, "Sensing with ultra-short Fabry–Perot cavities written into optical micro-fibers," *Sensors Actuators B, Chem.*, vol. 244, pp. 1016–1021, Jan. 2017.

[15] Y. Zheng *et al.*, "Fiber optic Fabry–Perot optofluidic sensor with a focused ion beam ablated microslot for fast refractive index and magnetic field measurement," *IEEE J. Sel. Topics Quantum Electron.*, vol. 23, no. 2, Jan. 2017, Art. no. 5601905.

[16] Q. Zhang, P. Hao, X. Tian, and Y. Li, "High-visibility in-line fiber-optic optofluidic Fabry–Pérot cavity," *Appl. Phys. Lett.*, vol. 111, no. 19, Nov. 2017, Art. no. 191102.

[17] D. Duan, Y. Rao, and T. Zhu, "High sensitivity gas refractometer based on all-fiber open-cavity Fabry–Perot interferometer formed by large lateral offset splicing," *J. Opt. Soc. Amer. B*, vol. 29, no. 5, pp. 912–915, Apr. 2012.

[18] J. Tian, Y. Lu, Q. Zhang, and M. Han, "Microfluidic refractive index sensor based on an all-silica in-line Fabry–Perot interferometer fabricated with microstructured fibers," *Opt. Express*, vol. 21, no. 5, pp. 6633–6639, Mar. 2013.

[19] M. Quan, J. Tian, and Y. Yao, "Ultra-high sensitivity Fabry–Perot interferometer gas refractive index fiber sensor based on photonic crystal fiber and Vernier effect," *Opt. Lett.*, vol. 40, no. 21, pp. 4891–4894, Nov. 2015.

[20] C. Wu, Z. Liu, A. P. Zhang, B. O. Guan, and H. Y. Tam, "In-line open-cavity Fabry–Pérot interferometer formed by C-shaped fiber for temperature insensitive refractive index sensing," *Opt. Express*, vol. 22, no.18, pp. 21757–21766, Sep. 2014.

[21] S. Gao *et al.*, "Microfiber-enabled in-line Fabry–Perot interferometer for high-sensitive force and refractive index sensing," *J. Lightw. Technol.*, vol. 32, no. 9, pp. 1682–1688, May 2014.

[22] X. Ni, S. Fu, and Z. Zhao, "Thin-fiber-based Fabry–Pérot cavity for monitoring microfluidic refractive index," *IEEE Photon. J.*, vol. 8, no. 3, May 2016, Art. no. 6803107.

[23] Y. Hou, T. Zhu, L. Shi, Q. Zhang, and K. S. Chiang, "Remote high temperature sensing with a reflective bandpass long-period fiber grating and a fiber ring laser," *Meas. Sci. Technol.*, vol. 24, Jul. 2013, Art. no. 094023.

[24] N. Song, C. Wu, W. Luo, Z. Zhang, and W. Li, "High strength fusion splicing of hollow core photonic crystal fiber and single-mode fiber by large offset reheating," *Opt. Fiber Technol.*, vol. 32, pp. 106–110, Nov. 2016.

[25] M. Tachikura, "Fusion mass-splicing for optical fibers using electric discharges between two pairs of electrodes," *Appl. Opt.*, vol. 23, pp. 492–498, Feb. 1984.

[26] L. H. Sheng, L. K. Yee, P. Y. Nan, Y. Y. Thung, Y. T. Khok, and F. A. Rahman, "Reinvestigation of the charge density distribution in arc discharge fusion system," in *2015 AIP Conf. Proc.*, 2015, Art.no. 040014.

[27] A. D. Yablon, *Optical Fiber Fusion Splicing*. Heidelberg, Germany: Springer-Verlag, 2005, ch. 3.

Qiang Zhang was born in Shanxi, China, in 1986. He received the B.S. degree in electronic science and technology from Guilin University of Electronic Technology, Guilin, China, in 2010 and the Ph.D. degree in optical engineering from Chongqing University, Chongqing, China, in 2015. He is currently a Lecturer with Shanxi University, Taiyuan, China. His research interests include optical fiber sensors, optofluidics, and optomechanics.

Zongyang Li received the B.E. degree in optical information science and technology in 2012 from Shanxi University, Taiyuan, China, where he is currently working toward the Ph.D. degree in optics.

Xinzhang Tian is currently working toward the B.E. degree in optical information science and technology from Shanxi University, Taiyuan, China.

Pengli Hao is currently working toward the B.E. degree in optical information science and technology from Shanxi University, Taiyuan, China.

Xuyang Wang was born in Shanxi, China, in 1984. He received the M.S. and Ph.D. degrees in physics from Shanxi University, Taiyuan, China, in 2010 and 2013, respectively. He is currently an Associate Professor with the Institute of Opto-Electronics, Shanxi University. His research interests include quantum optics and quantum communication.

Yongmin Li was born in Shanxi, China, in 1977. He received the B.S. degree in material physics and the Ph.D. degree in optics from Shanxi University, Taiyuan, China, in 1998 and 2003, respectively. He is currently a Professor with the Institute of Opto-Electronics, Shanxi University. His current research interest is quantum optics and quantum communication.